

Published in final edited form as:

Appl Opt. 2011 August 1; 50(22): 4310–4319.

Interpretation of dark-field contrast and particle-size selectivity in grating interferometers

Susanna K. Lynch¹, Vinay Pai¹, Julie Auxier², Ashley F. Stein³, Eric E. Bennett¹, Camille K. Kemble¹, Xianghui Xiao⁴, Wah-Keat Lee⁴, Nicole Y. Morgan¹, and Han Harold Wen^{1,*}

¹Lab of Imaging Physics, Translational Medicine Branch, National Heart, Lung and Blood Institute, National Institutes of Health, Bethesda, Maryland 20892, USA

²School of Chemical, Biological and Environmental Engineering, Oregon State University, Corvallis, Oregon 97331, USA

³Harvard Medical School, Boston, Massachusetts 02115, USA

⁴X-Ray Science Division, Advanced Photon Source, Argonne National Laboratory, Argonne, Illinois 60439, USA

Abstract

In grating-based x-ray phase sensitive imaging, dark-field contrast refers to the extinction of the interference fringes due to small-angle scattering. For configurations where the sample is placed before the beamsplitter grating, the dark-field contrast has been quantified with theoretical wave propagation models. Yet when the grating is placed before the sample, the dark-field contrast has only been modeled in the geometric optics regime. Here we attempt to quantify the dark-field effect in the grating-before-sample geometry with first-principle wave calculations and understand the associated particle-size selectivity. We obtain an expression for the dark-field effect in terms of the sample material's complex refractive index, which can be verified experimentally without fitting parameters. A dark-field computed tomography experiment shows that the particle-size selectivity can be used to differentiate materials of identical x-ray absorption.

1. Introduction

Grating-based x-ray phase sensitive imaging techniques generally employ a grating in the x-ray beam to produce a dense fringe pattern on the image plane at some distance downstream; changes in the position and amplitude of the fringes indicate x-ray refraction and coherent scattering in the sample (Fig. 1) [1–8]. The advantage of the grating approach is its ability to acquire full-field images using gratings of large areas. X-ray refraction and diffraction both arise from spatial variation of the refractive index in the sample material, but on different length scales. X-ray refraction is caused by macroscopic variations of the refractive index in the sample that are resolved by the imaging detector. Diffraction, or coherent scattering, is caused by unresolved, microscopic fluctuations of the refractive index. Coherent scattering causes angular divergence of the incident beam, which is observed in diffraction-enhanced imaging [9] and rigorously modeled by Nesterets [10].

In grating-based techniques, the scattering effect incurs a drop of the fringe amplitude in addition to the usual intensity attenuation caused by absorption. The additional fringe amplitude attenuation is represented by the dark-field image [6]. We showed in a previous paper that the fringe amplitude decays exponentially with the sample thickness in the

*Corresponding author: wenh@nhlbi.nih.gov.

geometric optics regime [7], and Yashiro *et al.* showed the same relationship in the Talbot interferometer configuration with the sample proceeding the beamsplitter grating [sample-before-grating (SbG) configuration] [11]. The fringe amplitude has also been modeled phenomenologically in dark-field computed tomography (CT) [12,13]. Specifically, if A is the fringe amplitude without any sample, and A' is the fringe amplitude when a sample of a single material and thickness T is in the beam, then the above models state that

$$A'/A = \exp(-\mu_a T - \mu_d T), \quad (1)$$

where μ_a is the absorption coefficient of the material and μ_d is the dark-field extinction coefficient (DFEC). The DFEC accounts for the effect of small-angle scattering on the fringes and is, by definition, the extinction coefficient of the fringe visibility V . The visibility is defined as the ratio of the fringe amplitude A over the average intensity J :

$$V = A/J. \quad (2)$$

The above relationship is illustrated in Fig. 2.

In coherent scattering, both the cross section and the angular distribution are dependent on the length scale of the scattering structures, so the dark-field extinction can potentially be used to characterize materials containing microscattering structures [14]. We showed in previous works [7,15] that the fringe visibility decays exponentially with the sample thickness when the fringes are geometric projections of Ronchi-type gratings and that the DFEC is determined by an autocorrelation of the electron density distribution. The correlation distance is determined by the device settings. In cases where wave interference must be considered, Yashiro *et al.* [11] analyzed Talbot interferometers in the SbG configuration [Fig. 1(a)]. They showed the exponential relationship with rigorous wave calculations, and they obtained the expression of the DFEC in terms of the autocorrelations of the complex refractive index.

An essential assumption shared by the Yashiro *et al.* model and the earlier Nesterets model is that the sample is illuminated by a plane wave. Under this assumption, the complex wave at any point on the wavefront can be expressed as a single-path integral through the sample along the direction of the beam. However, in the grating-before-sample (GbS) configuration with the grating proceeding the sample [16], the plane wave assumption no longer holds. The sample is now illuminated by a sum of plane waves at different angles. The transmitted wave involves the sum of projections along different paths in the sample. As a result, the derivations of Nesterets and Yashiro cannot be easily extended to obtain the DFEC.

Because the GbS geometry has certain practical advantages over the SbG geometry, it is worthwhile to obtain the DFEC for the GbS geometry. These advantages include the ease of grating fabrications [16] and lower radiation exposure when Ronchi-type intensity gratings are used [7,15,17–19]. We therefore obtained the theoretical expression of the DFEC for the GbS geometry using a stacked-slice model and wave propagation calculations.

The theoretical expression was then tested in aqueous suspensions of silica microspheres. In a 3D tomography experiment of iron-oxide particle suspensions, the dark-field image is shown to distinguish between materials of different microscopic composition but similar bulk absorption coefficients [20].

2. Theory of the GbS Geometry Dark-Field Extinction Coefficient

Our starting assumptions are the same as the ones by Nesterets and Yashiro, but without the plane wave assumption. These are (i) the short wavelength assumption—over the distance of the x-ray wavelength λ , the phase and absorption effects in the material are small and (ii) the small angle scattering assumption—if the typical size of the unresolved scatterers in the material is D , then $\lambda/D \ll 1$.

We denote the complex refractive index of the imaged sample as

$$n=1+\chi, \quad (3)$$

where

$$\chi=-\delta-i\beta, \quad (4)$$

where δ and β represent the phase shifts and magnitude attenuation in the material, respectively. The short wavelength assumption means that $|\chi| \ll 1$. We consider χ to contain a smooth (resolvable) part χ_s and a fine (unresolved) part χ_f [10]:

$$\chi=\chi_s+\chi_f. \quad (5)$$

We denote an x-ray wave vector as k :

$$k=2\pi/\lambda, \quad (6)$$

and k_x , k_y , and k_z are its Cartesian projections:

$$k_z=\sqrt{k^2-k_x^2-k_y^2}. \quad (7)$$

Let the incident beam come along the Z axis. Our basic model is to section the sample into a stack of thin slices of thickness t , along planes perpendicular to the Z axis (Fig. 3). Removing all material beyond the plane at z allows us to consider the incremental effect of a single slice t . We denote the fringe amplitude on the detector before adding the slice as $A(z)$, and after as $A(z+t)$. The average intensities on the detector before and after adding the slice are denoted as $J(z)$ and $J(z+t)$. The fringe visibility V is defined as the ratio A/J . If V to the leading order of t satisfies

$$V(z+t)-V(z)=-t\mu_d(z)V(z), \quad (8)$$

and μ_d is a parameter expressed in the fine fluctuation χ_f then the differential form of Eq. (8) is

$$\frac{dV(z)}{dz}=-\mu_d(z)V(z). \quad (9)$$

The solution to this equation is simply

$$V(z) = V(0) \exp \left[- \int_0^z \mu_d(\tau) d\tau \right]. \quad (10)$$

Equation (10) would mean that the fringe visibility decreases exponentially with the sample thickness by the coefficient μ_d , which is the DFEC that we want to solve.

To carry out this procedure, we first focus on the complex wave function at the entry plane z of the thin slice (the entry wave function) (see Fig. 3) and the complex wave function at the exit plane $z + t$ (exit wave function). The entry wave function is an integral sum of plane waves of a spread of wave vector \mathbf{k} 's. By the small-angle scattering assumption, $k_x/k \ll 1$ and $k_y/k \ll 1$. We denote the complex amplitude of wave vector (k_x, k_y, k_z) as $a(k_x, k_y)$, so that the entry wave function is

$$E(x, y, z) = \int dk_x dk_y a(k_x, k_y) \exp(-ik_x x - ik_y y - ik_z z). \quad (11)$$

The exit wave function can be expressed in terms of the entry wave function by the projection approximation under the short wavelength assumption [21]:

$$E(x, y, z+t) = \int dk_x dk_y a(k_x, k_y) \exp(-ik_x x - ik_y y - ik_z z) \times \exp[-i\Phi(k_x, k_y, x, y, z)], \quad (12)$$

where Φ is the phase delay and attenuation through the slice for each plane wave along its path:

$$\Phi(k_x, k_y, x, y, z) = \int_0^t d\tau \frac{k^2}{k_z} \chi \left(x - \frac{k_x}{k} \tau, y - \frac{k_y}{k} \tau, z + \tau \right). \quad (13)$$

Because we model the refractive index χ as the sum of smooth and fine parts [Eq. (5)], Φ also contains two parts:

$$\Phi(k_x, k_y, x, y, z) = \Phi_s(k_x, k_y, x, y, z) + \Phi_f(k_x, k_y, x, y, z), \quad (14)$$

where the fine part is explicitly

$$\Phi_f(k_x, k_y, x, y, z) = \int_0^t d\tau \frac{k^2}{k_z} \chi_f \left(x - \frac{k_x}{k} \tau, y - \frac{k_y}{k} \tau, z + \tau \right). \quad (15)$$

Now we expand χ_f to the leading order of k_x/k and k_y/k :

$$\chi_f \left(x - \frac{k_x}{k} \tau, y - \frac{k_y}{k} \tau, z + \tau \right) \approx \chi_f(x, y, z + \tau) - \frac{k_x}{k} \tau \frac{\partial \chi_f}{\partial x} - \frac{k_y}{k} \tau \frac{\partial \chi_f}{\partial y}. \quad (16)$$

Under the small-angle scattering assumption, if the typical size of the fluctuations in the fine part of the refractive index χ_f is D , then

$$\frac{k_x}{k}, \frac{k_y}{k} \sim \frac{\lambda}{D} \ll 1. \quad (17)$$

Substituting Eq. (17) into Eq. (16), and noting that the spatial derivatives of χ_f in the X and Y directions are on the order of χ_f/D , while τ is between 0 and t , we have

$$\chi_f\left(x-\frac{k_x}{k}\tau, y-\frac{k_y}{k}\tau, z+\tau\right)=\chi_f(x, y, z+\tau)\left[1+O\left(\frac{\lambda t}{D^2}\right)\right], \quad (18)$$

where $O(\lambda t/D^2)$ means a term on the order of $\lambda t/D^2$. Additionally, the k^2/k_z factor in Eq. (13) can be expanded by the Taylor series as

$$\frac{k^2}{k_z} \approx k \left[1 + \frac{1}{2} \left(\frac{k_x^2 + k_y^2}{k^2} \right) \right] = k \left[1 + O\left(\frac{\lambda^2}{D^2}\right) \right]. \quad (19)$$

Substituting Eqs. (18) and (19) into Eq. (15) yields

$$\Phi_f(k_x, k_y, x, y, z) = \int_0^t d\tau k \chi_f(x, y, z+\tau) \left[1 + O\left(\frac{\lambda^2}{D^2}\right) + O\left(\frac{\lambda t}{D^2}\right) \right]. \quad (20)$$

Now we can make the slice thickness t small enough such that $|\chi_f|kt \ll 1$ and $\lambda t/D^2 \ll 1$, then

$$\Phi_f(k_x, k_y, x, y, z) \approx \Phi_f(x, y, z), \quad (21)$$

where

$$\Phi_f(x, y, z) = k \int_0^t d\tau \chi_f(x, y, z+\tau). \quad (22)$$

Equation (22) means that in a thin slice and under the small-angle scattering assumption, the projection through the slice for the different plane waves can be approximated by a single projection along the Z direction.

We now substitute Eq. (21) into Eq. (14) and the result into Eq. (12) to simplify the expression of the wave on the exit plane:

$$E(x, y, z+t) = \exp[-i\Phi_f(x, y, z)] \int dk_x dk_y a(k_x, k_y) \exp(-ik_x x - ik_y y - ik_z z) \times \exp[-i\Phi_s(k_x, k_y, x, y, z)].$$

Note that if the fine part χ_f did not exist in the slice and only the smooth χ_s is present, then the exit wave function would be

$$E_s(x, y, z+t) = \int dk_x dk_y a(k_x, k_y) \exp(-ik_x x - ik_y y - ik_z z) \times \exp[-i\Phi_s(k_x, k_y, x, y, z)]. \quad (24)$$

So Eq. (23) means that the actual exit wave function with both χ_f and χ_s present can be expressed as a modification on the smooth wave function E_s (note that E_s still accounts for χ_f in the sample up to the entry plane of the slice):

$$E(x, y, z+t) = \exp[-i\Phi_f(x, y, z)] E_s(x, y, z+t). \quad (25)$$

We are now ready to calculate the fringe amplitude on the detector plane at position z_d . For horizontal fringes, the fringe amplitude is defined as

$$A = \frac{2}{\text{Area}} \int_{\text{detector}} dx_d dy_d I(\vec{r}_d) \exp(-igy_d), \quad (26)$$

where “Area” is the detector area illuminated by x rays, $I(\vec{r}_d)$ is the x-ray intensity at position \vec{r}_d on the detector plane, and $g = 2\pi/(\text{fringe period})$. The intensity $I(\vec{r}_d)$ is given by the wave function on the detector plane:

$$I(\vec{r}_d) = E(\vec{r}_d) E^*(\vec{r}_d). \quad (27)$$

We write the wave function on the detector plane $E(\vec{r}_d)$ in terms of the wave function on the exit plane of the thin slice $E(\vec{r})$ by a propagator P :

$$E(\vec{r}_d) = \int_{z \text{ plane}} dx dy E(\vec{r}) P(\vec{r}_d - \vec{r}). \quad (28)$$

Substituting Eq. (28) into Eq. (27) and the result into Eq. (26) gives an expression of the fringe amplitude in terms of the wave function at the exit plane:

$$\begin{aligned} A(z) &= \frac{2}{\text{Area}} \int_{\text{detector}} dx_d dy_d E(\vec{r}_d) E^*(\vec{r}_d) \exp(-igy_d) \\ &= 2 \int_{z \text{ plane}} dx_1 dy_1 dx_2 dy_2 E(\vec{r}_1) E^*(\vec{r}_2) \frac{1}{\text{Area}} \times \int_{\text{detector}} dx_d dy_d P(\vec{r}_d - \vec{r}_1) P^*(\vec{r}_d - \vec{r}_2) \exp(-igy_d) \\ &= 2 \int_{z \text{ plane}} dx_1 dy_1 dx_2 dy_2 E(\vec{r}_1) E^*(\vec{r}_2) Q(\vec{r}_1, \vec{r}_2), \end{aligned}$$

where the function Q is given by

$$Q(\vec{r}_1, \vec{r}_2) = \frac{1}{\text{Area}} \int_{\text{detector}} dx_d dy_d P(\vec{r}_d - \vec{r}_1) P^*(\vec{r}_d - \vec{r}_2) \exp(-igy_d). \quad (30)$$

Now we need to find an explicit form for the function Q in order to calculate the fringe amplitude. Under the small-angle scattering assumption expressed in Eq. (17), we use the Fresnel–Kirchhoff diffraction formula for the propagator P [22]:

$$P(\vec{r}_d - \vec{r}) = \frac{-i}{\lambda} \frac{\exp(-ik|\vec{r}_d - \vec{r}|)}{|\vec{r}_d - \vec{r}|}. \quad (31)$$

We now expand the propagator P with the Fresnel formula under the small-angle scattering assumption:

$$P(\vec{r}_d - \vec{r}) \approx \frac{-i}{\lambda} \frac{1}{(z_d - z)} \exp \left[-ik(z_d - z) - ik \frac{1}{z_d - z} \times \left(\frac{x_d^2 + y_d^2 + x^2 + y^2}{2} - x_d x - y_d y \right) \right], \quad (32)$$

and we substitute this back into Eq. (30) to obtain

$$Q(\vec{r}_1, \vec{r}_2) = \frac{1}{\text{Area}} \int_{\text{detector}} dx_d dy_d \frac{1}{\lambda^2 (z_d - z)^2} \times \exp \left\{ -ik \frac{1}{z_d - z} \left[\frac{x_1^2 + y_1^2 - x_2^2 - y_2^2}{2} - x_d(x_1 - x_2) - y_d(y_1 - y_2) \right] \right\},$$

where the distance d is given in terms of the fringe period p as

$$d = \frac{g}{k}(z_d - z) = \frac{\lambda}{p}(z_d - z). \quad (34)$$

Integrating Eq. (33) over the x_d and y_d on the detector plane results in a simple expression for Q :

$$Q(\vec{r}_1, \vec{r}_2) = \frac{1}{\text{Area}} \delta(x_1 - x_2) \delta(y_1 - y_2 - d) \times \exp \left[-ig \left(y_2 + \frac{d}{2} \right) \right]. \quad (35)$$

By substituting Eq. (35) into Eq. (29), we obtain the expression of the fringe amplitude in terms of the entry wave function before the slice is added:

$$A(z) = \frac{2}{\text{Area}} \int_{z \text{ plane}} dx dy E \left(\vec{r} + \frac{d}{2}, y \right) E^* \left(\vec{r} - \frac{d}{2}, y \right) \times \exp(-igy). \quad (36)$$

After adding the slice, the fringe amplitude can be written in terms of the exit wave function in the same way:

$$A(z+t) = \frac{2}{\text{Area}} \int_{z+t \text{ plane}} dx dy E \left(x, y + \frac{d}{2}, z+t \right) \times E^* \left(x, y - \frac{d}{2}, z+t \right) \exp(-igy). \quad (37)$$

Substituting the expression of the exit wave function in Eq. (25) into Eq. (37) leads to

$$A(z+t) = \frac{2}{\text{Area}} \int_{z+t \text{ plane}} dx dy \exp \left[-i\Phi_f \left(x, y + \frac{d}{2}, z \right) + i\Phi_f^* \left(x, y - \frac{d}{2}, z \right) \right] E_s \left(x, y + \frac{d}{2}, z+t \right) \times E_s^* \left(x, y - \frac{d}{2}, z+t \right) \exp(-igy).$$

Next, we define

$$\Delta\Phi_f(x, y, z) = \Phi_f \left(x, y + \frac{d}{2}, z \right) - \Phi_f^* \left(x, y - \frac{d}{2}, z \right). \quad (39)$$

Because we have made the slice thickness t sufficiently small such that $|\chi_f|kt \ll 1$, by Eq. (20) we have $\Delta\Phi_f(x, y, z) \ll 1$. Therefore, we write the Taylor series of $A(z+t)$ in Eq. (38) in terms of $\Delta\Phi_f(x, y, z)$:

$$A(z+t) \approx \frac{2}{\text{Area}} \int_{z+t \text{ plane}} dx dy \left[1 - i\Delta\Phi_f(x, y, z) - \frac{1}{2}\Delta\Phi_f^2(x, y, z) \right] E_s \left(x, y + \frac{d}{2}, z+t \right) E_s^* \left(x, y - \frac{d}{2}, z+t \right) \exp(-igy).$$

The leading term of the Taylor series in Eq. (40) is

$$A_s(z+t) = \frac{2}{\text{Area}} \int_{z+t \text{ plane}} dx dy E_s \left(x, y + \frac{d}{2}, z+t \right) E_s^* \left(x, y - \frac{d}{2}, z+t \right) \exp(-igy). \quad (41)$$

With Eq. (36) we recognize $A_s(z+t)$ as the fringe amplitude we would get if the slice only contained the smooth variation χ_s . This is a very useful fact in the following derivation.

The second term in the Taylor series of Eq. (40) is

$$\Delta A_1 = -i \frac{2}{\text{Area}} \int_{z+t \text{ plane}} dx dy \Delta \Phi_f(x, y, z) \times E_s \left(x, y + \frac{d}{2}, z+t \right) E_s^* \left(x, y - \frac{d}{2}, z+t \right) \exp(-igy). \quad (42)$$

Because $\Delta \Phi_f(x, y, z)$ is proportional to the fine fluctuation χ_f in the slice, and E_s contains only the smooth χ_s in the slice, the spatial fluctuation of $\Delta \Phi_f(x, y, z)$ is random relative to the rest of the integrand in Eq. (42). Therefore, only the average of $\Delta \Phi_f(x, y, z)$ in the XY plane contributes to the integral. If we denote the average in the XY plane as $\langle \rangle_{xy}$, then

$$\Delta A_1 = -i \langle \Delta \Phi_f(x, y, z) \rangle_{xy} \frac{2}{\text{Area}} \int_{z+t \text{ plane}} dx dy \times E_s \left(x, y + \frac{d}{2}, z+t \right) \times E_s^* \left(x, y - \frac{d}{2}, z+t \right) \exp(-igy). \quad (43)$$

Using the expression of $A_s(z+t)$ in Eq. (41), Eq. (43) is shortened to

$$\Delta A_1 = -i \langle \Delta \Phi_f(x, y, z) \rangle_{xy} A_s(z+t). \quad (44)$$

Because $\langle \chi_f \rangle_{xy} = 0$, we have

$$\langle \Delta \Phi_f(x, y, z) \rangle_{xy} = 0. \quad (45)$$

Therefore,

$$\Delta A_1 = 0. \quad (46)$$

The last term of the Taylor series in Eq. (40) is

$$\Delta A_2 = -\frac{1}{\text{Area}} \int_{z+t \text{ plane}} dx dy \Delta \Phi_f^2(x, y, z) \times E_s \left(x, y + \frac{d}{2}, z+t \right) E_s^* \left(x, y - \frac{d}{2}, z+t \right) \exp(-igy). \quad (47)$$

Again by the same reasoning leading to Eq. (43), we have

$$\Delta A_2 = -\langle \Delta \Phi_f^2(x, y, z) \rangle_{xy} \times \frac{1}{\text{Area}} \int_{z+t \text{ plane}} dx dy E_s \left(x, y + \frac{d}{2}, z+t \right) E_s^* \left(x, y - \frac{d}{2}, z+t \right) \exp(-igy). \quad (48)$$

Using Eq. (41), Eq. (48) is shortened to

$$\Delta A_2 = -\frac{1}{2} \langle \Delta \Phi_f^2(x, y, z) \rangle_{xy} A_s(z+t). \quad (49)$$

From the definition of $\Delta \Phi_f(x, y, z)$ in Eq. (39) and the definition of $\Phi_f(x, y, z)$ in Eq. (22), we can further write

$$\langle \Delta \Phi_f^2(x, y, z) \rangle_{xy} = k^2 \left\langle \left[\int_0^t d\tau_1 \chi_f \left(x, y + \frac{d}{2}, z+\tau_1 \right) - \int_0^t d\tau_2 \chi_f^* \left(x, y - \frac{d}{2}, z+\tau_2 \right) \right]^2 \right\rangle_{xy}. \quad (50)$$

We define a function $C(d, z)$ as

$$C(d, z) = \frac{1}{2t} \left\langle \left[\int_0^t d\tau_1 \chi_f \left(x, y + \frac{d}{2}, z + \tau_1 \right) - \int_0^t d\tau_2 \chi_f^* \left(x, y - \frac{d}{2}, z + \tau_2 \right) \right]^2 \right\rangle_{xy}, \quad (51)$$

then Eq. (50) is shortened to

$$\langle \Delta \Phi_f^2(x, y, z) \rangle_{xy} = 2k^2 C(d, z). \quad (52)$$

Substituting Eq. (52) into Eq. (49) yields

$$\Delta A_2 = -tk^2 C(d, z) A_s(z+t). \quad (53)$$

Finally, we collect all three terms in the Taylor series in Eq. (40) to obtain an expression of the fringe amplitude after the addition of the thin slice:

$$A(z+t) = A_s(z+t) [1 - tk^2 C(d, z)]. \quad (54)$$

To calculate the fringe visibility V , we still need to find the expression for the average intensity J on the detector plane. The average intensity on the detector is

$$J = \frac{1}{\text{Area}} \int_{\text{detector}} dx_d dy_d I(\vec{r}_d). \quad (55)$$

From Eq. (26) we recognize that the average intensity is equivalent to half of a hypothetical fringe amplitude when the fringe period is infinitely large. Correspondingly, the distance d defined in Eq. (34) is zero. So, the same expression derived for the fringe amplitude in Eq. (54) also applies to the intensity except that the distance d is now zero:

$$J(z+t) = J_s(z+t) [1 - tk^2 C(0, z)]. \quad (56)$$

The fringe visibility after the addition of the slice is, by definition, $V(z+t) = A(z+t)/J(z+t)$. Substituting Eq. (56) and (54) into this definition yields

$$\begin{aligned} V(z+t) &= \frac{A_s(z+t) [1 - tk^2 C(d, z)]}{J_s(z+t) [1 - tk^2 C(0, z)]} \\ &\approx V_s(z+t) \{1 - tk^2 [C(d, z) - C(0, z)]\}, \end{aligned} \quad (57)$$

where $V_s(z+t)$ is the fringe visibility if the refractive index of the slice only contains the smooth part χ_s . Because the smooth part is resolved by the detector and does not alter the fringe visibility, $V_s(z+t)$ is equal to the fringe visibility before adding the slice:

$$V_s(z+t) = V_s(z). \quad (58)$$

Substituting Eq. (58) into Eq. (57) yields

$$V(z+t) \approx V(z) \left\{ 1 - tk^2 [C(d, z) - C(0, z)] \right\}, \quad (59)$$

or

$$V(z+t) - V(z) \approx -tk^2 [C(d, z) - C(0, z)] V(z). \quad (60)$$

In differential form, this equation is equivalent to

$$\frac{dV(z)}{dz} = -k^2 [C(d, z) - C(0, z)] V(z), \quad (61)$$

and the solution is

$$V(z) = V(0) \exp \left\{ - \int_0^z k^2 [C(d, \tau) - C(0, \tau)] d\tau \right\}. \quad (62)$$

Thus we finally showed that in the GbS geometry, the fringe visibility also decreases exponentially with the sample thickness and the extinction coefficient at location z in the sample is

$$\mu_d(z) = k^2 [C(d, z) - C(0, z)]. \quad (63)$$

To express the DFEC in terms of the complex refractive index of the material χ , we substitute the definition of $C(d)$ in Eq. (51) into Eq. (63) to obtain

$$\begin{aligned} \mu_d(z) &= \frac{k^2}{2t} \left\{ \left[\int_0^t d\tau_1 \chi_f \left(x, y + \frac{d}{2}, z + \tau_1 \right) - \int_0^t d\tau_2 \chi_f^* \left(x, y - \frac{d}{2}, z + \tau_2 \right) \right]^2 - \left[\int_0^t d\tau_1 \chi_f \left(x, y, z + \tau_1 \right) - \int_0^t d\tau_2 \chi_f^* \left(x, y, z + \tau_2 \right) \right]^2 \right\}_{>_{xy}} \\ &= k^2 \left\{ \frac{1}{t} \left\langle \int_0^t d\tau_1 \int_0^t d\tau_2 \chi_f \left(x, y, z + \tau_1 \right) \times \chi_f^* \left(x, y, z + \tau_2 \right) \right\rangle_{>_{xy}} - \frac{1}{t} \left\langle \int_0^t d\tau_1 \int_0^t d\tau_2 \chi_f \left(x, y + \frac{d}{2}, z + \tau_1 \right) \times \chi_f^* \left(x, y - \frac{d}{2}, z + \tau_2 \right) \right\rangle_{>_{xy}} \right\}. \end{aligned} \quad (64)$$

We define an autocorrelation function of the fine part of the complex refractive index χ_f as

$$R(d, z) = \frac{1}{t} \left\langle \int_0^t d\tau_1 \int_0^t d\tau_2 \chi_f \left(x, y + \frac{d}{2}, z + \tau_1 \right) \times \chi_f^* \left(x, y - \frac{d}{2}, z + \tau_2 \right) \right\rangle_{>_{xy}}, \quad (65)$$

where d is the autocorrelation distance. Then, the final reduced expression of the DFEC is

$$\mu_d(z) = \frac{4\pi^2}{\lambda^2} [R(0, z) - R(d, z)]. \quad (66)$$

Experimentally, if the sample is made of a single type of material, then the DFEC is the same over the sample. It can be measured from the fringe visibility with the sample present (V') and without the sample (V):

$$\mu_d = -\frac{1}{T} \ln(V'/V), \quad (67)$$

where T is the thickness of the sample.

3. Applying to a Suspension of Microspheres of Uniform Diameter

We applied the above theory to obtain the DFEC of a random suspension of silica microspheres of diameter D in water. If the distance between the sample and the detector is L and the fringe period is p , then the autocorrelation distance d defined by Eq. (34) is $\lambda L/p$. If we denote the difference of the complex refractive index between silica and water as $\Delta\chi$, then Eqs. (66) and (65) lead to a closed-form expression of the DFEC:

$$\mu_d = \frac{3\pi^2}{\lambda^2} f |\Delta\chi|^2 d \begin{cases} D' - \sqrt{D'^2 - 1} (1 + D'^{-2}/2) + (D'^{-1} - D'^{-3}/4) \\ \ln[(D' + \sqrt{D'^2 - 1})/(D' - \sqrt{D'^2 - 1})], & \text{for } D > d; \\ D', & \text{for } D \leq d; \end{cases} \quad (68)$$

where f is the volume fraction of the microspheres and D' is the ratio D/d .

For hard x rays, the difference between the complex refractive indices of two materials is determined by the difference in the electron density $\Delta\rho$ and absorption coefficient $\Delta\mu$:

$$\Delta\chi = -r_e \lambda^2 \Delta\rho / 2\pi - i \lambda \Delta\mu / 2\pi, \quad (69)$$

where r_e is the classical electron radius of 2.82×10^{-15} m. Because both $\Delta\rho$ and $\Delta\mu$ are known, the DFEC can be evaluated directly from Eq. (68) and verified experimentally without any fitting parameters.

4. Experimental Test of the Theory

The experiments were performed at beamlines 32-ID and 2-BM of the Advanced Photon Source (APS) at the Argonne National Laboratory, Argonne, Ill. Four samples of microsphere suspensions were imaged, each containing $10 \mu\text{m}$ uniform silica microspheres of 2.0 g/cm^3 density and 0.15, 0.3, 0.5 or $1.5 \mu\text{m}$ diameters, separately. The experimental conditions are tabulated in Table 1. The samples were held in 0.5 ml centrifuge vials. The size of the x-ray beams were approximately 1.0 mm. Each vial was positioned, in turn, to center on the beam and imaged. On the 32-ID beamline, the $15 \mu\text{m}$ fringes were produced with a custom-fabricated silicon $\pi/2$ phase shift grating of $15 \mu\text{m}$ period. The grating was placed at one-fourth the Talbot distance from the detector. On the 2-BM beamline, a two-dimensional cross-grid Ronchi grating was used to produce the $78 \mu\text{m}$ fringes [23]. The Ronchi grating was a geological sieve woven of gold wires.

To obtain theoretical values of the DFEC from Eq. (68), the volume fraction f of the microspheres in a sample was determined from the measured intensity attenuation coefficient μ and the published values of water and silica by the United States National Institute of Standards and Technology (<http://physics.nist.gov/PhysRefData/FFast/html/form.html>):

$$f = (\mu - \mu_{\text{water}}) / (\mu_{\text{silica}} - \mu_{\text{water}}). \quad (70)$$

In order to plot data from different x-ray energies and microsphere diameters on the same graph, we calculated the normalized and unitless DFEC, which we define as

$$\mu_d' = \mu_d \lambda^2 / (3\pi^2 f |\Delta\chi|^2 d). \quad (d71)$$

By Eq. (68) μ_d' is only dependent on D' , which is the ratio of the microsphere diameter over the autocorrelation distance. We can therefore plot all data on a μ_d' versus D' graph.

The experimental values of the DFEC were computed from the fringe visibility according to Eq. (67). The fringe visibility was computed from the fringe amplitude according to its definition of (fringe amplitude)/(average intensity). The fringe amplitude and average intensity were in turn measured from the raw images according to Eq. (26) [7,15].

5. Results

In all four samples, the volume fraction of the microspheres ranged between 4% and 5%. The experimental DFEC and the theoretical curve are plotted in Fig. 4.

The measured data agreed with the theory over the entire range of experimental conditions. For a fixed volume fraction of the microspheres, the DFEC is seen to increase linearly with the microsphere diameter D when D is small relative to the autocorrelation length d . It peaks at $D = 1.8 d$, then decreases gradually for larger diameters. At the largest D/d ratio we tested, which was 12, the DFEC decreased to about 40% of the peak values. Generally, and in agreement with theory, the dark-field effect is biased toward larger microspheres.

6. 3D Tomography of an Iron-Oxide Nanoparticle Suspension

A common, water-based, acrylic black paint contains iron-oxide pigments (PBk11) of 0.1 to 0.2 μm size. X-ray diffraction by these pigments should give rise to the dark-field effect if the autocorrelation distance d of the imaging device is adjusted to the pigment size. We performed 3D tomography of samples containing a black paint (Liquitex Thin Body Mars Black) and 80 mg/ml KI solution in a laboratory scanner. The scanner consisted of a tungsten-target x-ray tube (Oxford XTG UltraBright) operating at 60 kVp and 40 W power, an x-ray camera consisting of a 16 bit water-cooled CCD array of matrix size 2045 \times 2048 and pixel size of 30 μm , coupled to a Gd2O2S:Tb phosphor screen via a 1:1 fiber-optic taper (PI-SCX-4096, Princeton Instruments), and a radiography Bucky grid acting as a Ronchi grating. The distance between the x-ray source focal spot and the camera was 2.0 m. The grating was placed exactly midway between the source and the camera, and the samples were held on a rotating stage 6 cm behind the grating. The period of the grating was 127 μm .

The fringe period was twice the grating period on the camera due to the projection magnification of the cone beam. The spectrum of the x-ray tube was broadly centered at 30 keV. The corresponding autocorrelation distance d in the DFEC expression [Eq. (66)] was 0.16 μm , matching the size of the pigments. A complete tomographic data set contained 180 projections of 1° increments each with 10 s exposure. Volumetric data of absorption and DFECs were obtained by processing the projections with a harmonic method in the Fourier domain [7,15] followed by projection/reconstruction.

The results are summarized in Fig. 5. The KI solution and acrylic paint attained the same level of x-ray absorption of 1.43 cm^{-1} . The acrylic paint had a DFEC of $1.32 \pm 0.14 \text{ cm}^{-1}$. This is significantly higher than the $0.67 \pm 0.05 \text{ cm}^{-1}$ value of the KI solution. However, the KI solution still had an apparent dark-field extinction rather than the null result one would expect from the theory due to the radiation hardening effect of the sample [24]. This effect can be corrected by placing a reference orthogonal grating in front of the camera, as was demonstrated previously [20].

7. Conclusion

We proved from first-principle wave calculations that under the short wavelength and small angle scattering assumptions, scattering by the sample media in GbS geometry grating interferometers results in exponential extinction of the interference fringe visibility relative

to the sample thickness. The same conclusion has been drawn previously for geometric optics [7,12] and SbG geometry interferometers [11]. We obtained an explicit expression of the DFEC and verified its accuracy in experiments with micro-sphere suspensions. Because our derivation was not specific to the way the fringes are produced, it also applies to other types of grating-based imaging techniques such as reflective grating Mach–Zehnder interferometers [25].

The expression of the DFEC shows particle-size selectivity: the DFEC is the strongest when the autocorrelation distance d is approximately equal to the radius of the scatterers. We can adjust the imaging device to meet this condition, and we thereby distinguish a material that contains particular scatterers from a uniform material, even though they have the same level of x-ray absorption.

A seeming contradiction between our expression of the DFEC and the general small-angle scattering consideration is that smaller particles produce larger scattering angles, and they may therefore be expected to cause a greater reduction of the fringe visibility or a higher extinction coefficient. But this is the opposite of the trend shown in Fig. 4 for particle sizes less than $1.8 d$. The explanation for this behavior is that the total amount of scattered x ray from a particle decreases rapidly with the size of the particle and offsets the effect of the larger scattering angle for sufficiently small sizes. Overall, the DFEC is related to structures that are too small to be directly resolved by the imaging detector. For this reason, it can be used for identifying materials of different microscopic composition in an imaging setting.

References

1. Yokozeki S, Suzuki T. Shearing interferometer using grating as beam splitter. *Appl Opt.* 1971; 10:1575–1580. [PubMed: 20111164]
2. David C, Nohammer B, Solak HH, Ziegler E. Differential x-ray phase contrast imaging using a shearing interferometer. *Appl Phys Lett.* 2002; 81:3287–3289.
3. Momose A, Kawamoto S, Koyama I, Hamaishi Y, Takai K, Suzuki Y. Demonstration of x-ray Talbot interferometry. *Jpn J Appl Phys.* 2003; 42:L866–L868.
4. Weitkamp T, Diaz A, David C, Pfeiffer F, Stamparoni M, Cloetens P, Ziegler E. X-ray phase imaging with a grating interferometer. *Opt Express.* 2005; 13:6296–6304. [PubMed: 19498642]
5. Takeda Y, Yashiro W, Suzuki Y, Aoki S, Hattori T, Momose A. X-ray phase imaging with single phase grating. *Jpn J Appl Phys.* 2007; 46:L89–L91.
6. Pfeiffer F, Bech M, Bunk O, Kraft P, Eikenberry EF, Bronnimann C, Grunzweig C, David C. Hard-x-ray dark-field imaging using a grating interferometer. *Nat Mater.* 2008; 7:134–137. [PubMed: 18204454]
7. Wen H, Bennett E, Hegedus MM, Carroll SC. Spatial harmonic imaging of x-ray scattering—initial results. *IEEE Trans Med Imaging.* 2008; 27:997–1002. [PubMed: 18672418]
8. Wang ZT, Kang KJ, Huang ZF, Chen ZQ. Quantitative grating-based x-ray dark-field computed tomography. *Appl Phys Lett.* 2009; 95:094105.
9. Wernick MN, Wirjadi O, Chapman D, Zhong Z, Galatsanos NP, Yang YY, Brankov JG, Oltulu O, Anastasio MA, Muehleman C. Multiple-image radiography. *Phys Med Biol.* 2003; 48:3875–3895. [PubMed: 14703164]
10. Nesterets YI. On the origins of decoherence and extinction contrast in phase-contrast imaging. *Opt Commun.* 2008; 281:533–542.
11. Yashiro W, Terui Y, Kawabata K, Momose A. On the origin of visibility contrast in x-ray Talbot interferometry. *Opt Express.* 2010; 18:16890–16901. [PubMed: 20721081]
12. Bech M, Bunk O, Donath T, Feidenhans'l R, David C, Pfeiffer F. Quantitative x-ray dark-field computed tomography. *Phys Med Biol.* 2010; 55:5529–5539. [PubMed: 20808030]

13. Jensen TH, Bech M, Zanette I, Weitkamp T, David C, Deyhle H, Rutishauser S, Reznikova E, Mohr J, Feidenhans'l R, Pfeiffer F. Directional x-ray dark-field imaging of strongly ordered systems. *Phys Rev B*. 2010; 82:214103.
14. Miller, EA.; White, TA.; McDonald, BS.; Seifert, A.; Flynn, MJ. Phase contrast x-ray imaging signatures for homeland security applications. *IEEE Nuclear Science Symposium and Medical Imaging Conference (2010 NSS/MIC)*; IEEE. 2011. p. 896-899.
15. Wen H, Bennett EE, Hegedus MM, Rapacchi S. Fourier x-ray scattering radiography yields bone structural information. *Radiology*. 2009; 251:910–918. [PubMed: 19403849]
16. Donath T, Chabior M, Pfeiffer F, Bunk O, Reznikova E, Mohr J, Hempel E, Popescu S, Hoheisel M, Schuster M, Baumann J, David C. Inverse geometry for grating-based x-ray phase-contrast imaging. *J Appl Phys*. 2009; 106:054703.
17. Olivo A, Speller R. A coded-aperture technique allowing x-ray phase contrast imaging with conventional sources. *Appl Phys Lett*. 2007; 91:074106.
18. Krejci F, Jakubek J, Kroupa M. Hard x-ray phase contrast imaging using single absorption grating and hybrid semiconductor pixel detector. *Rev Sci Instrum*. 2010; 81:113702. [PubMed: 21133473]
19. Morgan KS, Paganin DM, Siu KKW. Quantitative x-ray phase-contrast imaging using a single grating of comparable pitch to sample feature size. *Opt Lett*. 2011; 36:55–57. [PubMed: 21209685]
20. Stein AF, Ilavsky J, Kopace R, Bennett EE, Wen H. Selective imaging of nano-particle contrast agents by a single-shot x-ray diffraction technique. *Opt Express*. 2010; 18:13271–13278. [PubMed: 20588456]
21. Davis TJ. A unified treatment of small-angle x-ray-scattering, x-ray refraction and absorption using the Rytov approximation. *Acta Cryst*. 1994; 50:686–690.
22. Born, M.; Wolf, E. *Principles of Optics*. Cambridge Univ. Press; 1999. Kirchhoff's diffraction theory; p. 421-424.
23. Wen HH, Bennett EE, Kopace R, Stein AF, Pai V. Single-shot x-ray differential phase-contrast and diffraction imaging using two-dimensional transmission gratings. *Opt Lett*. 2010; 35:1932–1934. [PubMed: 20548343]
24. Wu XZ, Liu H. An experimental method of determining relative phase-contrast factor for x-ray imaging systems. *Med Phys*. 2004; 31:997–1002. [PubMed: 15191283]
25. Kemble CK, Auxier J, Lynch SK, Bennett EE, Morgan NY, Wen H. Grazing angle Mach-Zehnder interferometer using reflective phase gratings and a polychromatic, un-collimated light source. *Opt Express*. 2010; 18:27481–27492. [PubMed: 21197023]

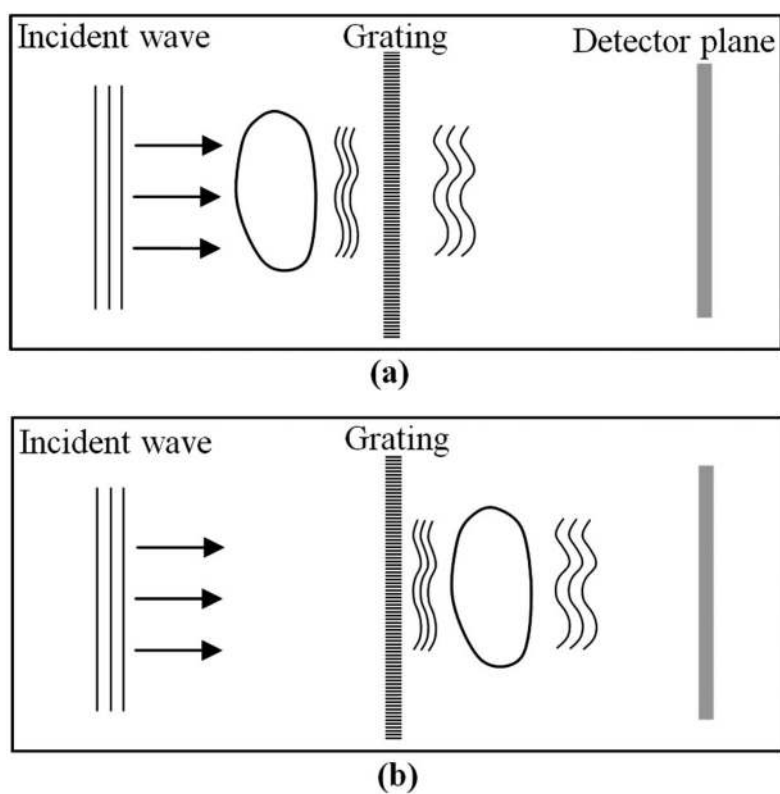


Fig. 1. Two different configurations of grating interferometers. (a) In the SbG geometry, a plane wave illuminates the sample and then the gratings. (b) In the GbS geometry, the plane wave is split by the grating into different directions of propagation and then transmitted through the sample.

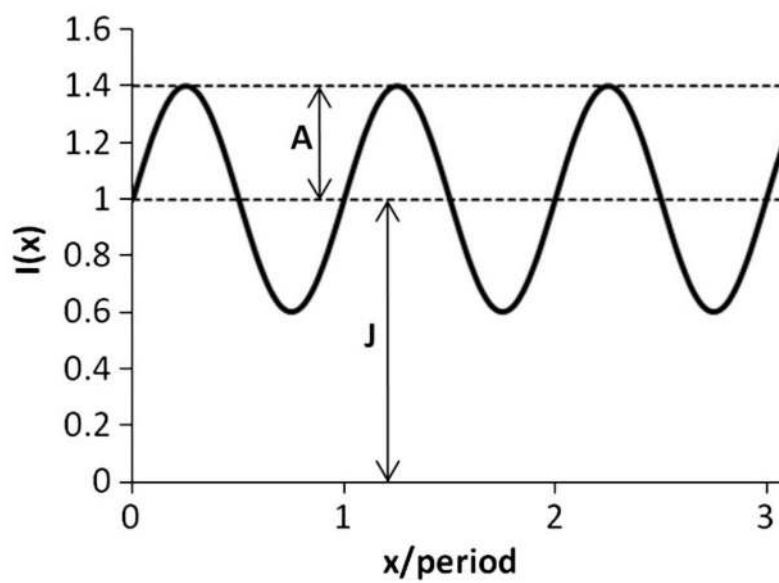


Fig. 2. Illustration of the fringe amplitude A and average intensity J of a fringe pattern on the detector screen. The fringe visibility V is defined as A/J .

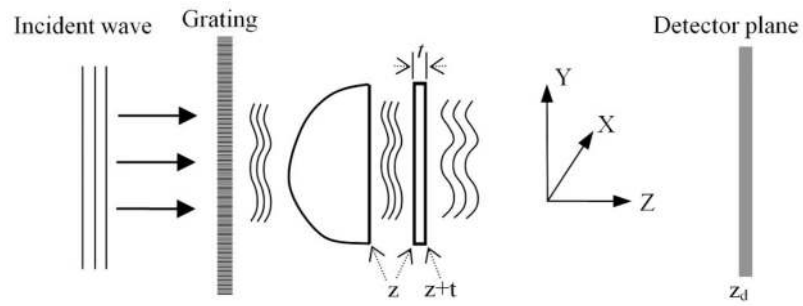


Fig. 3.

To model the DFEC in the GbS geometry, the imaged sample is sectioned into thin slices along the Z axis. The effect of a slice of thickness t at position z is analyzed by first removing all material beyond z , and then adding only the slice. The gap between the two surfaces of the section plane at z is artificially added to illustrate the entry wave into the slice.

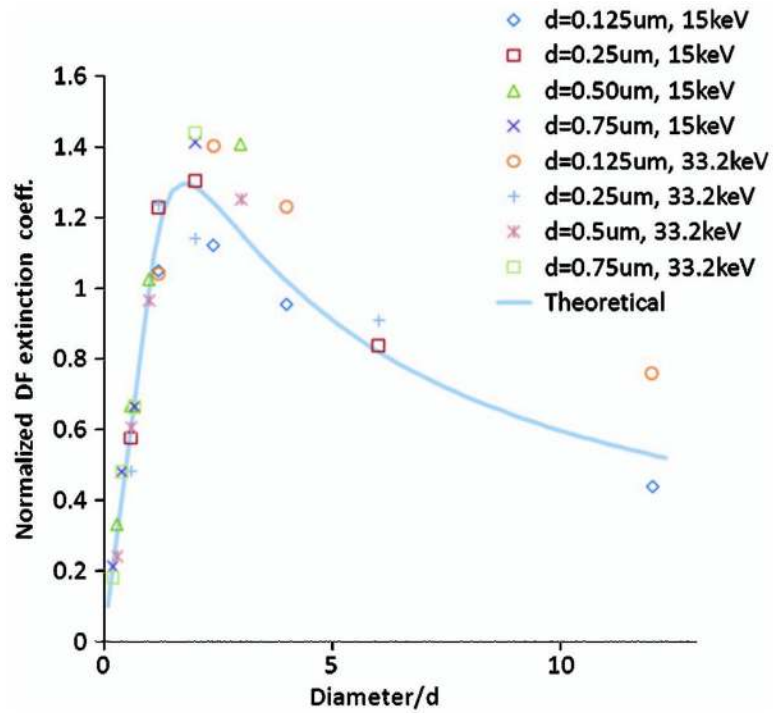


Fig. 4. Experimental and theoretical values of the unitless DFEC defined in Eq. (68). Because all parameters are known *a priori*, no fitting was involved.

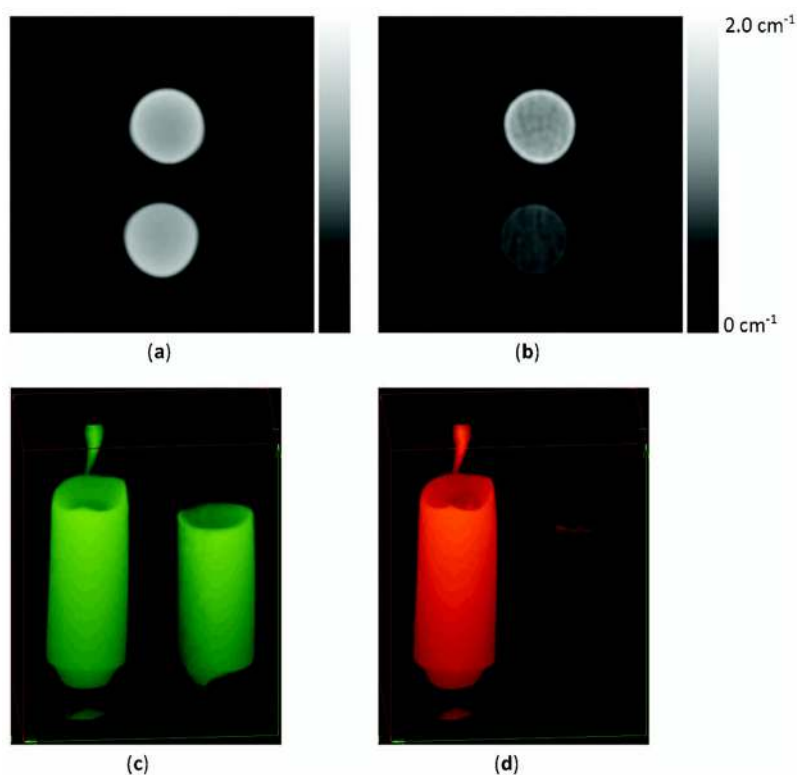


Fig. 5.

(a) Cross section of the volume CT data of absorption coefficient of two vials holding a black acrylic paint (on left) and 80 mg/ml KI solution, respectively, in units of cm^{-1} . (b) The same cross section showing the DFECs of the vials. (c) and (d) are semitransparent volume renditions of the absorption and DFEC, respectively. The vials have the same level of absorption, but x-ray scattering by the paint pigments causes a more visible dark-field effect.

Table 1

Experimental Conditions

	Sector 32-ID, 33.2 keV, 15 μm Fringe Period	Sector 2-BM, 15 keV, 78 μm Fringe Period
Autocorrelation Distance d (μm)	Sample-to-Detector Distance (cm)	Sample-to-Detector Distance (cm)
0.125	5.0	11.8
0.25	10.0	23.6
0.50	20.1	47.3
0.75	30.1	70.9